LASER & PHOTONICS REVIEWS
www.lpr-journal.org

Arbitrary Achromatic Polarization Control with Reconfigurable Metasurface Systems

*Evan W. Wang, Shang-Jie Yu, Thaibao Phan, Scott Dhuey, and Jonathan A. Fan**

Dynamic control over the polarization state of light is foundational for many scientific and technological applications, yet it remains a challenge to dynamically tailor responses with arbitrary polarization bases over a broad bandwidth. Broadband metasurface systems that utilize microscale displacements between two metasurfaces to enable reconfigurable polarization responses within a predefined polarization basis are reported. The metasurface pairs form an interferometer, and the lateral displacements produce detour phase shifts within the interferometer beam paths that mediate polarization state tuning. It is shown how the metasurface systems can be designed using freeform topology optimization to enable tailorable elliptical birefringence responses over a large bandwidth and how cascaded metasurface systems can enable the mapping of input and output polarization states between any two points on the Poincare sphere. It is anticipated that these concepts will have utility in imaging, display, communications, and metrology applications in classical and quantum optical domains.

Control over the polarization state of light is of great interest for a variety of applications including polarimetry,[1,2] quantum optics,[3] nonlinear optics,[4,5] optical trapping,[6] and biomedical imaging.[7,8] For many of these concepts, the required level of polarization control extends beyond simple manipulation within linear or circular polarization bases and can require transformations involving arbitrary elliptical polarization states. The current standard for specifying arbitrary elliptical polarization responses involves bulk devices, such as cascaded waveplates[9] or liquid crystal elements.[10] These concepts rely on intrinsic material birefringence and are difficult to tailor to arbitrary polarization bases. Additionally, dynamic modifications to the polarization response typically require the physical reconfiguration of bulky elements, which is slow.

Qualitatively new approaches to polarization control are needed to break these limitations. In this vein, metasurfaces have emerged as a new class of ultra-thin nanophotonic device featuring unprecedented polarization control.[11–13] With the metasurface paradigm, individual meta-atoms are utilized as nanoscale waveplates, and they can be symmetry broken in ways that enable polarization manipulation with engineered polarization bases. These meta-atoms can be stitched together to produce devices with complex polarization responses, from the generation of beams with angular momenta[14] to the routing of light as a function of polarization state[15] for polarimetry and quantum metrology applications. While the development of static metasurfaces for polarization control has matured, it remains a challenge to reconfigure these responses. Active metasurfaces based on liquid crystals,[16,17] phase change materials,[18,19] and field-effect refractive index tuning[20] have limits in capability and scalability, and they do not currently extend to arbitrary polarization control over large area devices.

In this work, we show how pairs of periodic metasurfaces, that is, metagratings, can be implemented to produce dynamically tunable elliptical and linear birefringent responses using microscale metagrating displacements. These concepts build on prior demonstrations of circular birefringence control in which pairs of geometric phase metasurfaces were mechanically displaced to produce reconfigurable polarization responses.[21] These concepts relied on the collective geometric phase response from full nanowaveplates specific to the circular polarization basis. In this study, we consider a more generalized framework for system configuration and the utilization of freeform, topology-optimized meta-atoms that support light–matter interactions with arbitrary polarization bases. We design and experimentally demonstrate pairs of metagratings that can support arbitrary birefringence responses, that is, rotations of an input polarization around an arbitrary axis on the Poincare sphere. We further show how cascaded pairs of metagrating systems can map an input polarization state to any point on the Poincare sphere, and we use these cascaded systems to produce output polarizations that dynamically scan the full Poincare sphere.

To understand how pairs of displaced metagratings can arbitrarily control polarization, we employ a broader framework than that discussed in ref. [21], which focused on phase responses based on full nanowaveplate symmetry breaking. We first consider here a normally incident plane wave on an individual metagrating. The incident wave can be generally described as the

E. W. Wang, S.-J. Yu, T. Phan, J. A. Fan
Department of Electrical Engineering
Stanford University
Stanford, CA 94305, USA
E-mail: jonfan@stanford.edu
S. Dhuey
Molecular Foundry
Lawrence Berkeley National Laboratory
Berkeley, California 94720, USA

The ORCID identification number(s) for the author(s) of this article can be found under https://doi.org/10.1002/lpor.202200926

DOI: 10.1002/lpor.202200926

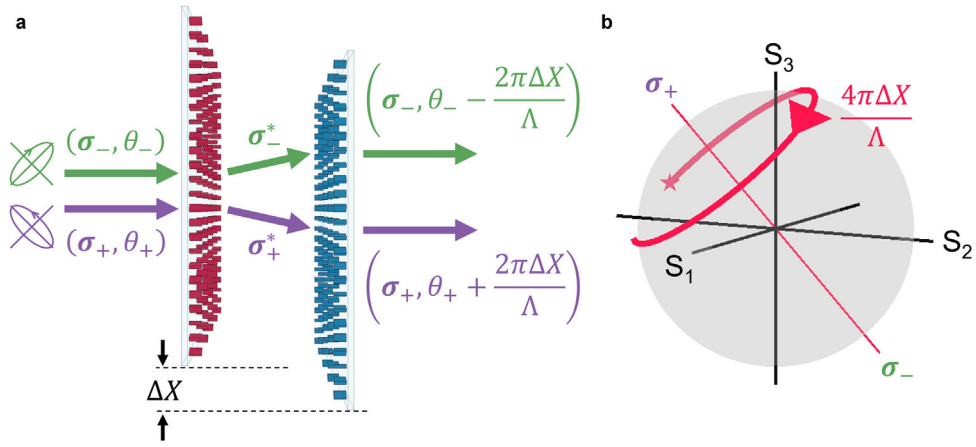

Figure 1. Polarization transformations with displaced metagrating systems. a) Schematic of the metagrating system. The incident beam can be described as a superposition of two beams, each with a characteristic polarization, $\boldsymbol{\sigma}$, and phase, θ. These beams diffract to different channels upon interacting with the first metagrating, and they recombine upon interacting with the second metagrating. The recombined beams accumulate a relative phase difference of $4\pi\Delta X/\Lambda$ due to detour phase shifts arising from ΔX. b) The phase difference accumulated between the two beams manifests as a rotation around an axis on the Poincare sphere with poles at $\boldsymbol{\sigma}_+$ and $\boldsymbol{\sigma}_-$. The initial polarization state is denoted by the red star.

superposition of two beams with orthogonal polarizations described by Jones vectors $\boldsymbol{\sigma}_+$ and $\boldsymbol{\sigma}_-$ and relative phases θ_+ and θ_-, respectively, at the metagrating interface. The metagrating diffracts the $\boldsymbol{\sigma}_+$ beam to the +1 order while simultaneously flipping its handedness to polarization state $\boldsymbol{\sigma}_+^*$, and it diffracts the $\boldsymbol{\sigma}_-$ beam to the −1 order while simultaneously flipping its handedness to polarization state $\boldsymbol{\sigma}_-^*$. The flipping of handedness upon diffraction is incorporated to ensure that this optical function can be feasibly realized with a single layer metasurface component.[22]

Two metagratings placed in series with parallel, mirror orientation form an interferometer. The first metagrating splits the incident beam to the +1 and −1 diffraction orders and the second metagrating diffracts and coherently recombines both beams back to the zeroth order to produce a normally transmitting beam (**Figure 1**a). Upon recombination, the polarization states of the beams revert back to the $\boldsymbol{\sigma}_+$ and $\boldsymbol{\sigma}_-$ basis due to reciprocity. The metasurfaces are oriented such that incident light illuminates the substrate side of the first metasurface and the nanostructure side of the second metasurface, which ensures that light travels through the substrate-air interfaces at normal incidence and any polarization transformations due to off-normal incidence at these interfaces are eliminated. When one of the metagratings undergoes a relative shearing displacement, phase differences between the two paths manifest as detour phase responses:[23–25] for a displacement ΔX and a metagrating period of Λ, light diffracted to the +1 order gains a phase of $2\pi\Delta X/\Lambda$ while light diffracted to the −1 order gains a phase of $-2\pi\Delta X/\Lambda$. Upon beam recombination via the second metagrating, the relative phase difference between the two overlapping beams is $4\pi\Delta X/\Lambda$ and manifests as a circumferential rotation around an axis on the Poincare sphere defined by $\boldsymbol{\sigma}_+$ and $\boldsymbol{\sigma}_-$ (Figure 1b).

Based on these considerations, our focal point for metasurface design is a metagrating that is capable of diffracting orthogonal polarization states to the +1 and −1 diffraction orders. Our approach builds on the formalism discussed in ref. [22] and utilizes meta-atoms that leverage both dynamic and geometric phase to specify phase and polarization response in a decoupled and independent manner. To briefly summarize, our desired Jones matrix, $\mathbf{J}(x)$, for a meta-atom at position x is

$$\mathbf{J}(x) = \left[e^{-i\phi_+(x)}\boldsymbol{\sigma}_+^* \;\; e^{-i\phi_-(x)}\boldsymbol{\sigma}_-^*\right]\left[\boldsymbol{\sigma}_+ \;\; \boldsymbol{\sigma}_-\right]^{-1} \tag{1}$$

$\phi_+(x)$ and $\phi_-(x)$ are functions of position and describe the linear phase fronts of a transmitted +1 and −1 diffracted beam, respectively. With the condition that the metagrating diffracts and flips beams with polarization states $\boldsymbol{\sigma}_+$ and $\boldsymbol{\sigma}_-$ to $\boldsymbol{\sigma}_+^*$ and $\boldsymbol{\sigma}_-^*$, respectively, $\mathbf{J}(x)$ can be diagonalized

$$\mathbf{J}(x) = \mathbf{R}(\theta)\begin{bmatrix} e^{-i\phi_{\text{fast}}} & 0 \\ 0 & e^{-i\phi_{\text{slow}}} \end{bmatrix}\mathbf{R}(-\theta) \tag{2}$$

In this form, the diagonal phase-only matrix corresponds to phase shifts within a linearly birefringent structure and the rotation matrices parameterized by θ correspond to axial structural rotations. The design objective becomes clear: each meta-atom is a linearly birefringent nanowaveplate rotated by θ with fast and slow axis phases of $e^{-i\phi_{\text{fast}}}$ and $e^{-i\phi_{\text{slow}}}$, respectively, and the final metagrating comprises many such nanowaveplates stitched together. We note that our meta-atoms are designed to transmit light to the zeroth diffracted order channel, and due to reciprocity, they have the same optical response upon illumination through the substrate or air. The metasurfaces will subsequently also perform the same functions for both illumination directions.

We consider the design of near-infrared metagratings made from single crystal silicon operating from wavelengths spanning 700 to 900 nm. The device is 500-nm-thick and contains 25 nanowaveplates each spaced by 420 nm per period, leading to $\Lambda = 10.5\mu$m. To enable broadband nanowaveplate responses, we utilize freeform topology optimization based on the adjoint variables method (AVM). AVM is an efficient technique for computing dielectric perturbations to a device in a manner that improves its performance, and it can couple with local or global gradient-based optimization algorithms to realize metasurface elements

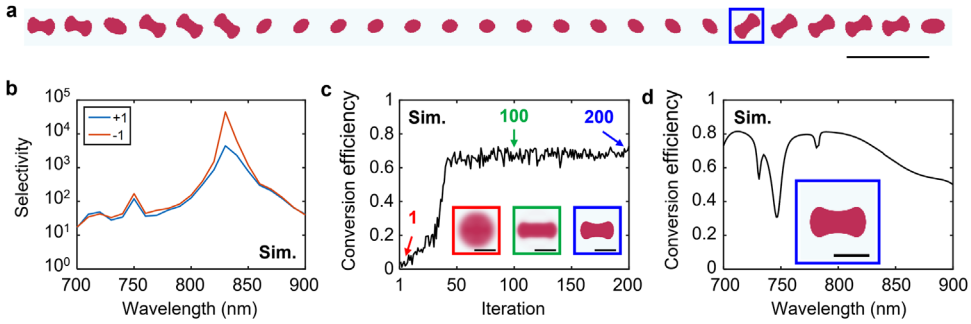

Figure 2. Elliptical polarization metagrating splitter. a) Layout of a single period of the freeform metagrating. Scale bar: 1 micron. b) Simulated selectivity for incident horizontally and vertically polarized light. c) Topology optimization trajectory of the nanowaveplate denoted by the blue box in (a). The conversion efficiency is averaged over wavelength. Insets: top views of the dielectric distribution of the nanowaveplate unit cell for the first, hundredth, and two hundredth iteration. Scale bar: 200 nm. d) Conversion efficiency of the final optimized nanowaveplate from (c) as a function of wavelength. Scale bar: 200 nm.

with exceptional efficiencies, bandwidths, and functionality.[26–29] Compared to conventionally designed meta-atom nanowaveplates based on basic rectangular shapes, which are intrinsically narrowband, freeform nanowaveplates with unusual topologies and curvilinear geometries are capable of producing polarization meta-elements with enhanced bandwidths[21] and even arbitrary polarization conversion.[30]

As proof-of-concept demonstrations, we design two types of broadband metagratings, one that can split horizontally and vertically polarized light to different diffraction orders and one that can split elliptical polarization states $\boldsymbol{\sigma}_+ = [1, -e^{-i\frac{\pi}{4}}]/\sqrt{2}$ and $\boldsymbol{\sigma}_- = [1, e^{-i\frac{\pi}{4}}]/\sqrt{2}$ to different diffraction orders.

One period of the fully optimized metagrating designed for elliptical polarization is shown in **Figure 2**a and shows an array of 25 freeform nanowaveplates. The device displays highly selective polarization-dependent diffraction across our wavelength band of interest (Figure 2b), indicating the efficacy of our design approach. To define selectivity, the device is illuminated with σ_+ (σ_-) polarized light and the σ_+ (σ_-) power in the +1 (−1) diffraction order is divided by the σ_- (σ_+) power in the +1 (−1) order.

A representative optimization trajectory of one of the nanowaveplates in the device, designed using periodic boundary conditions and simulated using rigorous coupled wave analysis,[31] is shown in Figure 2c and indicates how the initial grayscale dielectric distribution evolves to a binary structure supporting high polarization conversion efficiency. The polarization conversion efficiency is defined as the power of transmitted $\boldsymbol{\sigma}_+^*$ ($\boldsymbol{\sigma}_-^*$) polarized light divided by the power of incident $\boldsymbol{\sigma}_+$ ($\boldsymbol{\sigma}_-$) polarized light. Importantly, random structural rotations were introduced each iteration to reduce the impact of near-field coupling between neighboring nanowaveplates, ensuring that the nanowaveplates maintain proper functionality after rotation and stitching into the metagrating device. The polarization conversion efficiency of the optimal nanowaveplate as a function of wavelength (Figure 2d) displays a high efficiency with a broader bandwidth than that typical of conventional rectangular waveguides. Discussion of the metagrating configured for linear polarized light splitting is in Supporting Information.

Pairs of both types of polarization splitters are fabricated on substrates consisting of a single-crystal silicon layer bonded to a glass substrate. Single-crystal silicon is used due to its high refractive index and relatively low absorption in the near-infrared.[32] The devices are patterned using electron beam lithography followed by reactive ion etching into the silicon layer. More details pertaining to the fabrication procedure are in the Supporting Information. Scanning electron micrographs of the fabricated linear and elliptical polarization splitters are shown in **Figures 3**a and 3c, respectively, and show excellent patterning fidelity and straight side walls in line with the ideally designed patterns.

To optically characterize the devices, polarization selectivity is experimentally measured for each metagrating. A white light laser coupled to a monochrometer serves as the incidence source and polarization filters specify the incident polarization and serve as polarization analyzers for the diffracted beams. The resulting selectivities across all wavelengths for both devices are plotted in Figure 3b,d, and we find that out fabricated metagratings have selectivities that are consistently greater than 10:1. We attribute the reduction in performance, compared to the simulated results, to fabrication imperfections arising from lithographic proximity errors and surface roughness in the etched silicon nanostructures, as well as deviations of the illumination setup from an ideal, normally incident plane wave.

The reconfigurable waveplate systems are implemented by configuring two identical metagratings in series alignment and mounting one of the metagratings on a motorized translation stage. In practice, the metagratings are implemented within a 4f system (**Figure 4**a), which enables blocking of the zeroth order transmission from the first metagrating to ensure the interferometer contains only the +1 and −1 orders as its two beams. The mechanism of detour phase modulation for interferometer tuning remains the same except for an added sign flip in the accumulated phase shift between σ_+ and σ_- upon beam recombination.

For the linear birefringent system comprising horizontal and vertical polarization splitters, the system is illuminated with diagonally polarized light, which is an equal superposition of the horizontal and vertical eigenpolarizations of the system. The transmitted horizontal, vertical, diagonal, and circular polarization components are measured as a function of metagrating displacement and incident wavelength. Linear birefringence is calculated by computing the transmitted Stokes vector from a

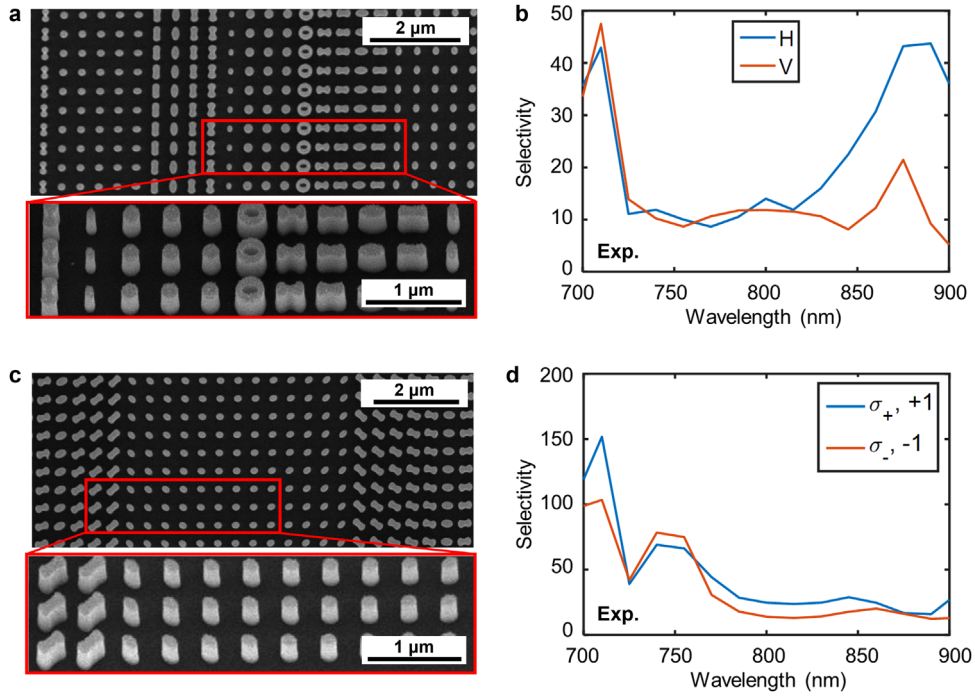

Figure 3. Fabricated metagrating polarization splitters. a,c) Scanning electron micrographs of fabricated a) linear polarization and c) elliptical polarization splitting metagratings. b,d) Experimentally measured selectivity for the b) linear (H, +1; V, −1) and d) elliptical polarization splitting metagratings.

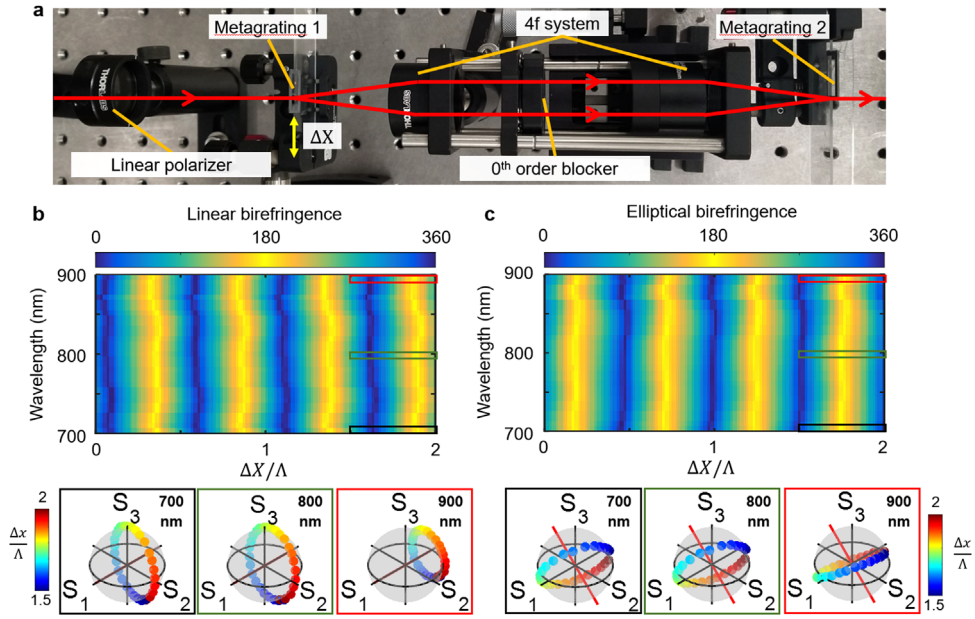

Figure 4. Experimental characterization of birefringent metagrating systems. a) Image of the optical setup comprising two metagratings within a 4f system. The first metagrating is mounted on a motorized stage and can undergo displacements of Δ*X*. The interfering beam paths within the interferometric system are shown in red. b,c) Measured b) linear and c) elliptical birefringence as a function of displacement and wavelength. The Poincare spheres show polarization state as a function of displacement for 700, 800, and 900 nm wavelengths.

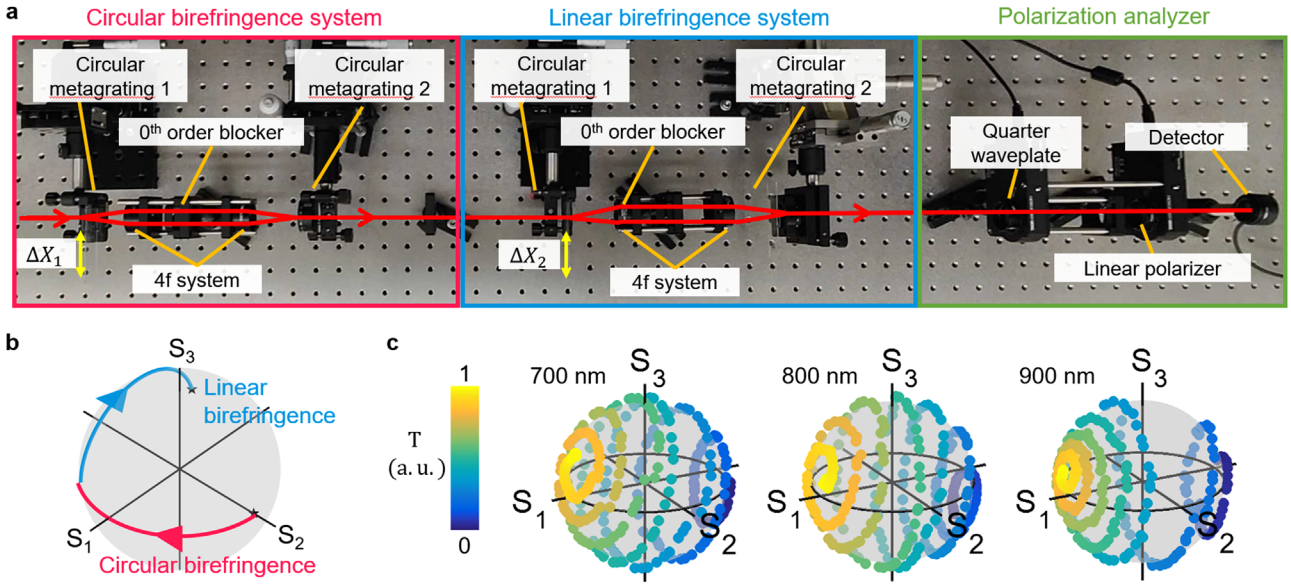

Figure 5. Arbitrary polarization control with cascaded metagrating systems. a) Top view of the optical setup showing the cascading of four metagratings each supporting reconfigurable circular and linear birefringence responses, respectively. b) Schematic of trajectories on the Poincare sphere enabled by circular and linear birefringence control. c) Experimentally measured polarization trajectories over time in arbitrary units for metagrating displacements intended to produce a spiral shape on the Poincare sphere, for 700, 800, and 900 nm wavelengths.

polarization-resolved transmission measurement, converting it to a Jones vector $\mathbf{P}$, and decomposing the Jones vector along the H–V polarization basis: $A_+ = \begin{bmatrix}1 & 0\end{bmatrix}\mathbf{P}$, $A_- = \begin{bmatrix}0 & 1\end{bmatrix}\mathbf{P}$. Linear birefringence is then defined as the phase of A_+/A_-. We note this expression describes the rotation of the polarization state around a target axis and not the full polarization state. Variations in the amplitude of A_+ and A_- can lead to aberrations in the actual polarization state path compared to ideal, as discussed below.

The plot on the left of Figure 4b shows the linear birefringence across all measured wavelengths and displacements and is uniform across our wavelength range. The birefringence has $\Lambda/2$ periodicity with displacement, which is consistent with our expectation from detour phase accumulation within our interferometric system and confirms that microscale metagrating motions can completely modulate linear birefringence. The fully polarized portion of the Stokes vectors at 700, 800, and 900 nm wavelengths are plotted on the Poincare sphere as a function of displacement in Figure 4b and show a vertically orientated great circle in the S_2–S_3 plane, which is the expected polarization transformation. At 700 and 800 nm, the system has nearly ideal behavior with only minor tilt, likely due to slight misalignment in the system. At 900 nm, there is visible aberration in the polarization transformation, manifested as an offsetting of the polarization transformation path from the great circle. This likely arises due to asymmetric selectivities (Figure 3b) and transmission amplitudes between the two polarizations at longer wavelengths.

A similar analysis is performed for the elliptically birefringent metasurface system. The system is illuminated with horizontally polarized light and various transmitted polarization amplitudes are measured using a set of polarization analyzers. In line with our calculation of linear birefringence, we compute the elliptical birefringence by converting the measured polarization states to Stokes vectors, converting those vectors to Jones vectors, and decomposing the vectors along the $\boldsymbol{\sigma}_+$ and $\boldsymbol{\sigma}_-$ basis: $B_+ = \boldsymbol{\sigma}_+^\dagger \mathbf{P}$ and $B_- = \boldsymbol{\sigma}_-^\dagger \mathbf{P}$. Elliptical birefringence, specified as the phase of B_+/B_-, is plotted in Figure 4d and shows clear birefringence across all measured wavelengths and displacements. The fully polarized portion of the output Stokes vector at 700, 800, and 900 nm wavelengths (Poincare spheres, Figure 4d) visualizes the expected polarization rotation around the axis defined by $\boldsymbol{\sigma}_+$ and $\boldsymbol{\sigma}_-$ at its poles.

Finally, we show that fully arbitrary polarization state transformations can be achieved by cascading two sets of metasurface systems together. Such polarization functionality is particularly important for metrology applications such as polarimetry and ellipsometry. This level of polarization control can be achieved using pairs of metasurface systems that utilize orthogonal axes around which to rotate polarization. For this demonstration, we use a circular birefringent system followed by a linear birefringent system (**Figure 5**a), in which the input linear polarization is first transformed via latitudinal rotations along the Poincare sphere, followed by longitudinal rotations (Figure 5b). The positions of the two translated metagratings required to generate an particular desired polarization state is

$$\Delta x_1 = -\frac{\Lambda_1}{4\pi}\cos^{-1} S_1 \tag{3}$$

$$\Delta x_2 = -\frac{\Lambda_2}{4\pi}\cos^{-1}\frac{S_2}{\sqrt{1-S_1^2}} \tag{4}$$

To characterize the system, a horizontally-polarized incident beam is used, the circular and linear birefringent systems undergo a sequence of Δx_1 and Δx_2 displacements, and the

transmitted polarization state is analyzed. Figure 5c shows the fully polarized portion of the Stokes vector plotted on the Poincare sphere for a set of stage movements specified to produce a spiral pattern. These plots show that with proper specification of microscale motions within the metasurface system, the input polarization state can be transformed to any other point on the Poincare sphere within the bandwidth of our system. Deviations from an ideal spiral pattern are evident at a wavelength of 900 nm, likely due to the same sources of nonidealities in the experimental system discussed earlier.

In summary, we have shown that pairs of polarization-functional metagratings can serve as dynamically tunable elliptically birefringent optical systems with tailorable polarization bases. These systems operate as interferometers that transduce microscale shear displacements between metagratings to modulated detour phase responses within each optical path, leading to shear-dependent birefringence. A design method based on the freeform optimization of birefringent meta-atoms enables broadband operation. Experimental demonstrations of linear and elliptical birefringent systems, together with a four metagrating system capable of supporting fully arbitrary polarization transformations, indicate the experimental potential of the concept.

Significant improvements in system performance and reductions in system form factor can be enabled with improved design and fabrication. Improvements in system performance are best addressed by improving the efficiencies of individual metasurfaces, which can be accomplished in multiple ways. First, design concepts that utilize advanced global optimization algorithms[33–36] to perform the freeform design of full metagrating periods[37–40] can produce devices with enhanced efficiencies and bandwidths beyond the limits of devices based on stitched meta-atoms. Second, multi-layer[41,42] or volumetric[43] freeform metasurfaces support large design landscapes with the potential to enable devices featuring near-unity efficiencies. Improved fabrication will ensure that experimental devices perform with metrics matching theoretical predictions. The experimental implementation of such high quality freeform metasurfaces has particular promise at longer wavelengths such as the mid-infrared[44] and terahertz,[45] where device feature sizes scale with wavelength and are less sensitive to fabrication issues such as proximity error. Alternatively, plasmonic metasurfaces with relatively high fabrication tolerance[46,47] can also be utilized. Further systems miniaturization and the potential for high speed polarization control can be enabled by implementing sheared metasurfaces using microelectromechanical systems.[48,49] We also envision that detour phase modulation can extend to aperiodic metasurface systems[50] to enable spatially-dependent polarization control and more generally dynamic wavefront control.

Supporting Information

Supporting Information is available from the Wiley Online Library or from the author.

Acknowledgements

The authors acknowledge support from NASA under Award 80NSSC21K0220, the AFOSR under Award FA9550-18-1-0070, and the Packard Fellowship Foundation. E.W.W. acknowledges support from the Stanford Graduate Fellowship. Work at the Molecular Foundry was supported by the Office of Science, Office of Basic Energy Sciences, of the US Department of Energy under Contract DE-AC02-05CH11231. Part of this work was performed at the nano@Stanford labs, which are supported by the NSF as part of the National Nanotechnology Coordinated Infrastructure under Award ECCS-1542152, and Stanford Nano Shared Facilities, supported by the NSF under Award ECCS-2026822.

Conflict of Interest

The authors declare no conflict of interest.

Data Availability Statement

The data that support the findings of this study are available from the corresponding author upon reasonable request.

Keywords

birefringence, dynamic control, metasurfaces, metagrating, polarization, Poincare spheres

Received: November 30, 2022
Revised: March 1, 2023
Published online: April 11, 2023

[1] W.-L. Hsu, G. Myhre, K. Balakrishnan, N. Brock, M. Ibn-Elhaj, S. Pau, *Opt. Express* **2014**, *22*, 3063.
[2] N. A. Rubin, G. D'Aversa, P. Chevalier, Z. Shi, W. T. Chen, F. Capasso, *Science* **2019**, *365*, eaax1839.
[3] R. Kopold, D. B. Milosevic, W. Becker, *Phys. Rev. Lett.* **2000**, *84*, 3831.
[4] V. V. Strelkov, A. A. Gonoskov, I. A. Gonoskov, M. Y. Ryabikin, *Phys. Rev. Lett.* **2011**, *107*, 043902.
[5] A. Fleischer, O. Kfir, T. Diskin, P. Sidorenko, O. Cohen, *Nat. Photonics* **2014**, *8*, 543.
[6] M. E. Friese, T. A. Nieminen, N. R. Heckenberg, H. Rubinsztein-Dunlop, *Opt. Lett.* **1998**, *23*, 1.
[7] S. P. Morgan, I. M. Stockford, *Opt. Lett.* **2003**, *28*, 114.
[8] A. Da Silva, C. Deumie, I. Vanzetta, *Biomed. Opt. Express* **2012**, *3*, 2907.
[9] E. Hecht, *Optics*, Addison-Wesley, Boston, MA **2002**.
[10] J. Nicolás, J. Campos, M. J. Yzuel, *J. Opt. Soc. Am. A* **2002**, *19*, 1013.
[11] A. Arbabi, Y. Horie, M. Bagheri, A. Faraon, *Nat. Nanotechnol.* **2015**, *10*, 937.
[12] Q. Song, S. Khadir, S. Vézian, B. Damilano, P. D. Mierry, S. Chenot, V. Brandli, P. Genevet, *Sci. Adv.* **2021**, *7*, eabe1112.
[13] Y. Hu, X. Wang, X. Luo, X. Ou, L. Li, Y. Chen, P. Yang, S. Wang, H. Duan, *Nanophotonics* **2020**, *9*, 3755.
[14] H. Ren, X. Fang, J. Jang, J. Bürger, J. Rho, S. A. Maier, *Nat. Nanotechnol.* **2020**, *15*, 948.
[15] K. Wang, J. G. Titchener, S. S. Kruk, L. Xu, H.-P. Chung, M. Parry, I. I. Kravchenko, Y.-H. Chen, A. S. Solntsev, Y. S. Kivshar, D. N. Neshev, A. A. Sukhorukov, *Science* **2018**, *361*, 1104.
[16] D. Shrekenhamer, W.-C. Chen, W. J. Padilla, *Phys. Rev. Lett.* **2013**, *110*, 177403.
[17] S.-Q. Li, X. Xu, R. M. Veetil, V. Valuckas, R. Paniagua-Domínguez, A. I. Kuznetsov, *Science* **2019**, *364*, 1087.
[18] Y. Wang, P. Landreman, D. Schoen, K. Okabe, A. Marshall, U. Celano, H.-S. P. Wong, J. Park, M. L. Brongersma, *Nat. Nanotechnol.* **2021**, *16*, 667.

[19] Y. Zhang, C. Fowler, J. Liang, B. Azhar, M. Y. Shalaginov, S. Deckoff-Jones, S. An, J. B. Chou, C. M. Roberts, V. Liberman, M. Kang, C. Ríos, K. A. Richardson, C. Rivero-Baleine, T. Gu, H. Zhang, J. Hu, *Nat. Nanotechnol.* **2021**, *16*, 661.
[20] G. K. Shirmanesh, R. Sokhoyan, P. C. Wu, H. A. Atwater, *ACS Nano* **2020**, *14*, 6912.
[21] E. W. Wang, T. Phan, S.-J. Yu, S. Dhuey, J. A. Fan, *Proc. Natl. Acad. Sci.* **2022**, *119*, e2122085119.
[22] J. P. Balthasar Mueller, N. A. Rubin, R. C. Devlin, B. Groever, F. Capasso, *Phys. Rev. Lett.* **2017**, *118*, 113901.
[23] M. Khorasaninejad, A. Ambrosio, P. Kanhaiya, F. Capasso, *Sci. Adv.* **2016**, *2*, e1501258.
[24] Z.-L. Deng, J. Deng, X. Zhuang, S. Wang, T. Shi, G. P. Wang, Y. Wang, J. Xu, Y. Cao, X. Wang, X. Cheng, G. Li, X. Li, *Light: Sci. Appl.* **2018**, *7*, 78.
[25] D. Wen, J. J. Cadusch, J. Meng, K. B. Crozier, *Adv. Funct. Mater.* **2020**, *30*, 1906415.
[26] J. Jensen, O. Sigmund, *Laser Photonics Rev.* **2011**, *5*, 308.
[27] C. M. Lalau-Keraly, S. Bhargava, O. D. Miller, E. Yablonovitch, *Opt. Express* **2013**, *21*, 21693.
[28] S. Molesky, Z. Lin, A. Y. Piggott, W. Jin, J. Vucković, A. W. Rodriguez, *Nat. Photonics* **2018**, *12*, 659.
[29] D. Sell, J. Yang, S. Doshay, R. Yang, J. A. Fan, *Nano Lett.* **2017**, *17*, 3752.
[30] Z. Shi, A. Y. Zhu, Z. Li, Y.-W. Huang, W. T. Chen, C.-W. Qiu, F. Capasso, *Sci. Adv.* **2020**, *6*, eaba3367.
[31] J. P. Hugonin, P. Lalanne, arXiv:2101.00901, **2021**.
[32] D. Sell, J. Yang, S. Doshay, K. Zhang, J. A. Fan, *ACS Photonics* **2016**, *3*, 1919.
[33] J. Jiang, J. A. Fan, *Nano Lett.* **2019**, *19*, 5366.
[34] J. Jiang, J. A. Fan, *Nanophotonics* **2020**, *9*, 1059.
[35] J. Jiang, J. A. Fan, *Nanophotonics* **2021**, *10*, 361.
[36] M. Chen, R. Lupoiu, C. Mao, D.-H. Huang, J. Jiang, P. Lalanne, J. A. Fan, *ACS Photonics* **2022**, *9*, 3110.
[37] E. Gershnabel, M. Chen, C. Mao, E. W. Wang, P. Lalanne, J. A. Fan, *ACS Photonics* **2022**. https://doi.org/10.1021/acsphotonics.2c01160
[38] D. Sell, J. Yang, E. W. Wang, T. Phan, S. Doshay, J. A. Fan, *ACS Photonics* **2018**, *5*, 2402.
[39] E. W. Wang, D. Sell, T. Phan, J. A. Fan, *Opt. Mater. Express* **2019**, *9*, 469.
[40] D. Sell, J. Yang, S. Doshay, J. A. Fan, *Adv. Opt. Mater.* **2017**, *5*, 1700645.
[41] Z. Lin, B. Groever, F. Capasso, A. W. Rodriguez, M. Lončar, *Phys. Rev. Appl.* **2018**, *9*, 044030.
[42] J. Fan, D. Sell, J. Yang, US10725290B2, **2017**.
[43] Q. Huang, L. T. Gan, J. A. Fan, *Adv. Mater.* **2023**, *35*, 2204688.
[44] G. Cao, H.-X. Xu, L.-M. Zhou, Y. Deng, Y. Zeng, S. Dong, Q. Zhang, Y. Li, H. Yang, Q. Song, X. Liu, Y. Li, C.-W. Qiu, *Mater. Today* **2021**, *50*, 499.
[45] W. Mo, X. Wei, K. Wang, Y. Li, J. Liu, *Opt. Express* **2016**, *24*, 13621.
[46] A. Hassanfiroozi, Y. Cheng, S. Huang, Y. Lin, P. Huang, Y. Shi, P. C. Wu, *Laser Photonics Rev.* **2022**, *16*, 2100525.
[47] J. Zhang, M. ElKabbash, R. Wei, S. C. Singh, B. Lam, C. Guo, *Light: Sci. Appl.* **2019**, *8*, 53.
[48] X. Zhao, J. Schalch, J. Zhang, H. R. Seren, G. Duan, R. D. Averitt, X. Zhang, *Optica* **2018**, *5*, 303.
[49] E. Arbabi, A. Arbabi, S. M. Kamali, Y. Horie, M. Faraji-Dana, A. Faraon, *Nat. Commun.* **2018**, *9*, 812.
[50] T. Phan, D. Sell, E. W. Wang, S. Doshay, K. Edee, J. Yang, J. A. Fan, *Light: Sci. Appl.* **2019**, *8*, 48.